


Low lattice thermal conductivity in Zintl phases Na₂AuBi and Na₂AuSb: An *ab initio* study

Mohd Zeeshan, Chandan Kumar Vishwakarma , and B. K. Mani*

Department of Physics, Indian Institute of Technology, Hauz Khas, New Delhi 110016, India

 (Received 19 February 2022; revised 29 July 2022; accepted 3 August 2022; published 22 August 2022)

In search of new prospects for room temperature thermoelectric applications, we computationally investigated the electronic structure and transport properties of Zintl phases Na₂AuBi and Na₂AuSb. We find remarkably low room temperature lattice thermal conductivity of 0.46 and 0.73 W m⁻¹ K⁻¹ for Na₂AuBi and Na₂AuSb, respectively. The proposed values are competitive with the record figure of merit material SnSe. We have demonstrated that such low thermal conductivity finds its origin majorly in low phonon group velocities and short phonon lifetime, arising from atomic displacements and lattice anharmonicity. We further predict a high figure of merit, i.e., $ZT \sim 1$ at 300 K for *p*-type Na₂AuBi. The value is further improved to $ZT \sim 1.8$ with spin-orbit coupling. We hope through this work we could shed light on two potential Zintl phases which would motivate further experimental investigations.

DOI: [10.1103/PhysRevMaterials.6.085404](https://doi.org/10.1103/PhysRevMaterials.6.085404)

I. INTRODUCTION

With the help of first-principles simulations, we can design new materials to address the current world issues [1–3]. Certain major challenges across the globe include increasing energy demand and climate changes [4]. In tackling these challenges, smart materials can play an important role. One of the promising candidates could be the thermoelectric materials [5]. These materials are known for directly converting waste heat into electricity [6]. The ability to scavenge the waste heat and simultaneously provide electricity makes them crucial for future technology as an alternate source of power generation [7]. However, scanning the literature reveals that despite significant advances in the field, there is an urgent need for thermoelectric materials with improved performances [8–15].

One of the major hurdles in designing efficient thermoelectrics could be attributed to the conflicting parameters in the figure of merit, $ZT = S^2\sigma T/\kappa$, where κ is the thermal conductivity with both electronic (κ_e) and lattice contributions (κ_L), S is Seebeck coefficient and σ is electrical conductivity [16]. It is challenging to decouple these conflicting parameters. Interestingly, the lattice thermal conductivity is nearly independent of the electronic part and opens the window for optimization. Recent research activities in thermoelectrics have emphasized on finding the materials with intrinsically low lattice thermal conductivity [17]. Some of the reported materials with low lattice thermal conductivity, thereby high ZT , belongs to a special class known as Zintl phases.

Zintl phases, to name a few, InTe [18], TlSe [19], Ca₅Al₂Sb₆ [20], NaCoO₂ [21], TlInTe₂ [22], and Yb₁₄MnSb₁₁ [23] are known to have intrinsically low thermal conductivity and accordingly high thermoelectric figure of merit. The room temperature lattice thermal conductivity (in W m⁻¹ K⁻¹) was reported to be around

0.65 for TlSe, 0.6 in the case of Ca₅Al₂Sb₆, and as low as 0.46 for TlInTe₂, which are significantly low in comparison to traditional thermoelectric materials. Such low thermal conductivities in Zintl phases are attributed to the large Grüneisen parameter, lattice anharmonicity, hierarchical bonding, rattling modes, low sound velocities, and high atomic displacement parameters [17,18,22]. Moreover, these phases offer compositions with small band gaps [24], complex structures [25], and dispersive bands [1]—favorable for thermoelectrics.

Intrigued by versatile properties within the Zintl phases, we searched for potential thermoelectric candidates and choose pnictides based Zintl phases Na₂AuBi and Na₂AuSb as the subject of this study. This choice is partly driven by experiments and partly by computational predictions. Both materials are synthesized by direct reaction of elements at elevated temperatures (700 °C), indicating high temperature sustainability [26,27]. In addition, based on electronic fitness function (EFF), Xing *et al.* demonstrated the favorable band complexity in Na₂AuBi as compared to other ternary systems [28]. However, EFF deals qualitatively with the electronic aspect only. The absence of crucial thermal transport and quantitative evaluation of electrical transport parameters renders Na₂AuBi little explored as a potential thermoelectric material. It can thus be surmised that there is a need for understanding the thermal transport of Na₂AuBi. A systematic theoretical study to understand the underlying mechanism can provide a roadmap to enhance the thermoelectric properties in these materials. Thus it will be interesting to see if Na₂AuBi and Na₂AuSb can show exceptionally low κ_L like other Zintl phases. And what are the factors which could govern low κ_L .

In this work, using first-principles calculations, we have demonstrated the low thermal conductivity in Na₂AuBi and Na₂AuSb. To account for such low values, we have examined the atomic displacements of the constituent atoms and phonon dynamics—band structure, group velocities, lifetime, and Grüneisen parameter. Electrical transport properties are calculated to obtain a comprehensive estimate of the thermo-

*bkmani@physics.iitd.ac.in

electric figure of merit. Throughout the paper, as our interest lies in room temperature thermoelectric applications, we have focused on the properties at 300 K. The paper is organized as follows: Sec. II discusses briefly the computational methods employed in the calculations, Sec. III presents the results of electrical and thermal transport, and finally, a summary of the paper is presented in Sec. IV.

II. COMPUTATIONAL METHODS

We carried out the density functional theory based first-principles simulations using the Vienna *ab initio* simulation package (VASP) [29,30] to obtain the equilibrium lattice constants, atomic positions, and electronic structure properties of Na_2AuBi and Na_2AuSb . The exchange-correlations among electrons were incorporated using the generalized gradient approximation (GGA) based Perdew-Burke-Ernzerhof (PBE) pseudopotential [31]. The plane-wave bases with an energy cutoff of 500 eV were used in all the calculations. The crystal structures were optimized using full relaxation calculations with help of a conjugate gradient algorithm with Monkhorst-Pack k mesh of $11 \times 11 \times 11$. The energy convergence and atomic forces criteria were used as 10^{-8} eV and 10^{-7} eV/Å, respectively. The self-consistent-field (SCF) calculations were performed using a dense k mesh of $21 \times 21 \times 21$. To examine the effect of spin-orbit coupling (SOC), we also performed the full-relativistic calculations.

We constructed a $2 \times 2 \times 2$ supercell (128 atoms) to calculate the phonon dispersions, second- and third-order interatomic force constants (IFCs), and the lattice thermal conductivity. The phonon dispersions were calculated with Γ -centered k mesh of $2 \times 2 \times 2$ using density functional perturbation theory (DFPT) as implemented in PHONOPY [32]. The second-order harmonic and third-order anharmonic IFCs were obtained using the finite-displacement method using PHONO3PY [33]. Utilizing the second- and third-order IFCs, the lattice thermal conductivity was obtained by solving the Boltzmann transport equation within the single-mode relaxation time approximation. The convergence of lattice thermal conductivity was tested using increasing q -mesh sizes, and a q mesh of $11 \times 11 \times 11$ was found to be optimal. The mean square displacements were derived from the number of phonon excitations, and the Grüneisen parameter was extracted using phonon calculations at equilibrium, larger (+2%) and smaller (-2%) volumes. The reported atomic displacements and Grüneisen parameters were tested for convergence with respect to q mesh.

The electrical transport properties were calculated using a k grid of $11 \times 11 \times 11$. We, however, did test calculations to assess the convergence in terms of increasing k grids. We found a negligible change in the electrical transport properties. The Seebeck coefficient, electrical conductivity, and the electronic thermal conductivity, were obtained by solving the Boltzmann transport equation as implemented in the AMSET code [34]. The scattering rate was calculated using four different mechanisms, acoustic deformation potential (AD), piezoelectric (PIE), polar optical phonon (POP), and ionized impurity (IMP) scattering.

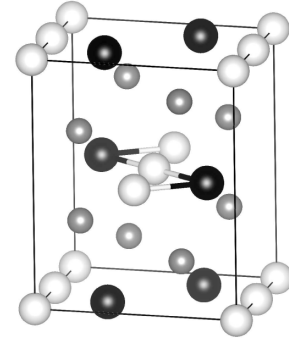


FIG. 1. Crystal structure of Na_2AuBi and Na_2AuSb in $Cmcm$ symmetry. Gray, white, and black colors represent the Na, Au, and Bi, respectively. The zigzag chains of Au and Sb/Bi are along c axis.

III. RESULTS AND DISCUSSIONS

In this section, we present and analyze our results on the structural, thermal transport, and electrical transport properties of Na_2AuBi and Na_2AuSb Zintl phases.

A. Structural optimization and electronic structure

Na_2AuBi and Na_2AuSb crystallize in an orthorhombic $Cmcm$ symmetry, the crystal structure is shown in Fig. 1. The Wyckoff positions for Na, Au, and pnictogen atoms Sb/Bi are $8g$ ($x, y, 1/4$), $4a$ ($1/2, 1/2, 0$), and $4c$ ($1/2, y, 1/4$), respectively. Au and Sb/Bi form zigzag chains along the c axis, whereas alkali atoms present on either side well separate the two neighboring chains [26]. The Na atoms are slightly more inclined towards the pnictogen atom along a axis, which indicates more interaction with Sb/Bi as compared to Au. To determine the ground state properties of Na_2AuBi and Na_2AuSb , the crystal structures were optimized by minimizing the total energy as a function of volume and atomic positions. The optimized lattice parameters and band gaps of the ground state structure are listed in Table I. As we observe from the table, the calculated parameters are in good agreement with experimental values, with a maximum discrepancy of 0.1 \AA in the case of lattice parameters whereas the maximum deviation in atomic positions is merely 0.01. The optimized unit cell is slightly elongated along the a and c axes and marginally compressed along the b axis, leading to a slightly overestimated volume. This can be attributed to the fact that GGA overestimates the lattice parameters [35]. Nevertheless, the calculated band gaps for Na_2AuBi and Na_2AuSb are 0.30 and 0.33 eV, respectively. Since the materials comprise heavy elements Au, Sb, and Bi, we also considered the relativistic effects in our simulations. The PBE-SOC has reduced the band gap to 0.14 and 0.23 eV, respectively. Importantly, the band gap survives in both the cases. In order to obtain a more accurate band gap, we employed modified Becke-Johnson (mBJ) exchange-correlation potential [36]. The corrected band gaps obtained are 0.89 and 0.97 eV for Na_2AuBi and Na_2AuSb , respectively. To the best of our knowledge, there are no data on experimental band gaps for both the materials. These optimized structural parameters are then used to calculate the electronic structures of the materials.

TABLE I. Calculated lattice parameters, band gaps, and Wyckoff positions for Na₂AuBi and Na₂AuSb in *Cmcm* symmetry. Experimental values mentioned in parentheses are taken from the Refs. [26,27] for Na₂AuBi and Na₂AuSb, respectively.

System	<i>a</i> (Å)	<i>b</i> (Å)	<i>c</i> (Å)	<i>E_g</i> (eV)			Wyckoff Positions				
				PBE	PBE-SOC	mBJ					
Na ₂ AuBi	9.54 (9.44)	7.66 (7.70)	5.94 (5.84)	0.30	0.14	0.89	Na	8 <i>g</i>	0.17 (0.16)	0.31 (0.31)	0.25 (0.25)
							Au	4 <i>a</i>	0 (0)	0 (0)	0 (0)
							Bi	4 <i>c</i>	0 (0)	0.31 (0.30)	0.75 (0.75)
Na ₂ AuSb	9.33 (9.27)	7.53 (7.56)	5.91 (5.84)	0.33	0.23	0.97	Na	8 <i>g</i>	0.32 (0.32)	0.33 (0.33)	0.25 (0.25)
							Au	4 <i>a</i>	0.5 (0.5)	0 (0)	0 (0)
							Sb	4 <i>c</i>	0 (0)	0.20 (0.20)	0.25 (0.25)

In Fig. 2, we present the electronic structure of Na₂AuBi [panels (a) and (b)] and Na₂AuSb [panels (d) and (e)]. For GGA-PBE bands, as we observe from panel (a), Na₂AuBi is an indirect semiconductor with valence-band maximum (VBM) at Γ and conduction-band minimum (CBM) at (0, 0.1316, 0) along the Γ -*S* direction. Interestingly, the difference between VBM (at *X*) and VBM-1 (at *S*) bands is less than 0.1 eV. Thus the bands at Γ , *X*, and *S* points may facilitate the charge carrier transport, thereby, improving the electrical conductivity [37]. It is well-known that degenerate bands help improve power factor [38,39]. We obtained such degenerate bands in VBM and CBM. On the other hand, as discernible from panel (d), Na₂AuSb is a direct band gap semiconductor with both VBM and CBM at Γ point. It exhibits similar bands like that of Na₂AuBi, on account of similar structures.

The electronic bands with mBJ-potential show similar topology, of course, with improved band gaps. On the other hand, the bands with PBE-SOC are shifted towards the Fermi level, resulting in the reduced band gaps. The effect is more pronounced in the case of Na₂AuBi. The curvature and slope of the bands have changed more in the valence band region of Na₂AuBi. This is expected to affect the electrical transport properties which we have discussed in the later section. Though the electronic structure provides a good insight into the electrical transport properties, the exact figure of merit depends on the collective behavior of the coupled parameters *S*, σ and κ_e .

To get further insight into it, we computed and analyzed the atom-projected density of states (PDOS). As discernible from panels (c) and (f), we observe the dominant contribution

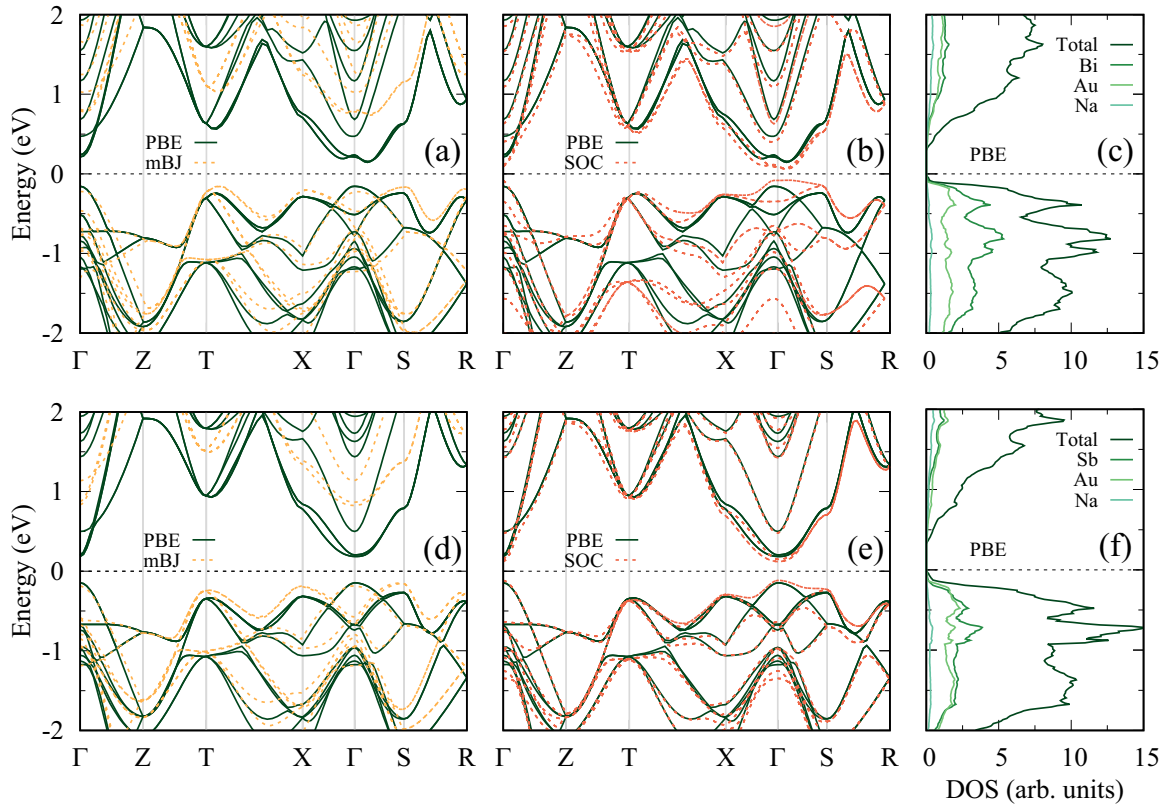


FIG. 2. Calculated [(a), (b) and (d), (e)] electronic band structures and [(c) and (f)] density of states of Na₂AuBi and Na₂AuSb, respectively, in *Cmcm* symmetry using PBE, PBE-SOC, and mBJ potential. For clarity, only the PBE density of states are shown.

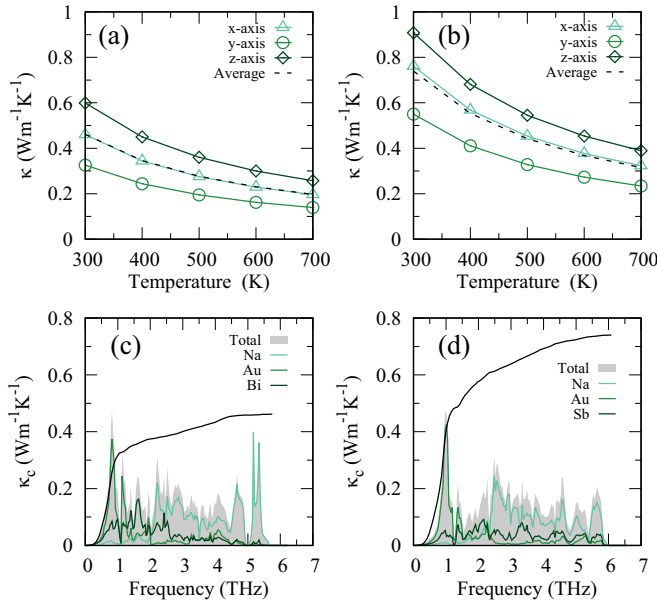


FIG. 3. Calculated [(a) and (b)] lattice thermal conductivity as a function of temperature and [(c) and (d)] cumulative lattice thermal conductivity as a function of phonon frequencies at 300 K for Na_2AuBi and Na_2AuSb , respectively. Superimposed are the phonon density of states in arbitrary units.

from Au atoms in VBM for Na_2AuBi , whereas the states of both Au and Sb contribute almost equally to VBM in the case of Na_2AuSb . Further, while the CBM has the similar contribution from Au and Sb/Bi, the contribution of Na remains negligible for both materials.

B. Lattice thermal conductivity

Next, we examine the lattice thermal conductivity, κ_L , in the considered thermoelectrics. For this, we solve the linearized phonon Boltzmann transport equation within the single-mode relaxation time approximation (RTA) as well as using direct solution as implemented in PHONO3PY [33]. However, no significant change in κ_L is observed. Therefore the further results for κ_L are presented within the RTA approach only. The κ_L , in RTA, is expressed as

$$\kappa_L = \frac{1}{NV} \sum_{\lambda} C_{\lambda} \mathbf{v}_{\lambda} \otimes \mathbf{v}_{\lambda} \tau_{\lambda}, \quad (1)$$

where N , V , C , \mathbf{v} , and τ represent the number of unit cells in the supercell, volume of the unit cell, heat capacity, phonon group velocity, and single-mode relaxation time, respectively. The index λ represents the phonon mode.

In Fig. 3, we have shown the lattice thermal conductivity as a function of temperature. As discernible from the figure, for both the Zintl phases, we observe a trend of decreasing lattice thermal conductivity as a function of temperature. The anisotropic crystal structure of the materials makes it customary to have different κ_L along different crystallographic axes. For both the materials, the contribution along the c axis is maximum whereas it is observed to be minimum along the b axis. The contribution along the a axis almost mirrors the average κ_L in

the case of both materials. The average κ_L of Na_2AuBi and Na_2AuSb range 0.46–0.19 and 0.73–0.31 $\text{W m}^{-1} \text{K}^{-1}$, respectively, in the temperature range 300–700 K. Interestingly, the values are significantly low and of the order of some lowest reported κ_L values. The average room temperature lattice thermal conductivity of Na_2AuBi ($\kappa_L = 0.46 \text{ W m}^{-1} \text{K}^{-1}$) and Na_2AuSb ($\kappa_L = 0.73 \text{ W m}^{-1} \text{K}^{-1}$) are comparable to some of the promising thermoelectric materials such as SnSe ($\kappa_L \sim 0.47 \text{ W m}^{-1} \text{K}^{-1}$) [40] and TlSe ($\kappa_L \sim 0.65 \text{ W m}^{-1} \text{K}^{-1}$) [19], respectively. Moreover, since κ_L decreases with increasing temperature and these materials can easily sustain 700 °C, the low values of κ_L at high temperatures further substantiate the thermoelectric potential of the proposed materials.

To understand the origin of such exceptionally low κ_L , next, we examine the phonon dispersion. The phonons are obtained by solving the equation (as implemented in PHONOPY [32])

$$\sum_{\beta\tau'} D_{\tau\tau'}^{\alpha\beta}(\mathbf{q}) \gamma_{\mathbf{q}j}^{\beta\tau'} = \omega_{\mathbf{q}j}^2 \gamma_{\mathbf{q}j}^{\alpha\tau}. \quad (2)$$

Here, the indices τ , τ' represent the atoms, α , β are the Cartesian coordinates, \mathbf{q} is a wave vector and j is a band index. $D(\mathbf{q})$ refers to as the dynamical matrix, and ω and γ are the corresponding phonon frequency and polarization vector, respectively. The phonon dispersion and corresponding DOS from our simulations are shown in panels (a), (d), and (b), (e) of Fig. 4 for Na_2AuBi and Na_2AuSb , respectively. As discernible from the dispersion curves, for both the materials, we do not observe any imaginary frequencies, which confirms the dynamical stability of the systems. The acoustic modes are dominated by Au atoms in both the systems, with some contribution from the pnictogen atom Sb/Bi, and negligible contribution from the alkali atom, Na. The mid-frequency and high-frequency optical modes are mostly occupied by alkali atom, Na. The phonon curves range 0 to 5.76 THz for Na_2AuBi and 0 to 6.08 THz in the case of Na_2AuSb , which suggests low frequency vibrations. Such low-lying phonon modes are indicative of low κ_L and are reminiscent of good thermoelectric materials such as SnSe (5.6 THz) [41], TlInTe_2 (5.9 THz) [19], and Bi_2Te_3 (4.6 THz) [42]. The acoustic phonons span less than 1.20 THz in both materials. The major contribution to κ_L stems from the acoustic modes, $\sim 76\%$ in Na_2AuBi and $\sim 70\%$ in Na_2AuSb . The contribution from high frequency optical phonons is negligible. This we have shown in panels (c) and (d) of Fig. 3. Since the contribution to acoustic phonons is dominated by Au, it is clear that the majority of κ_L originates from the Au atoms.

Another important feature to observe is a gap in phonon dispersion around 4.9 THz for Na_2AuBi which hints at low κ_L [43]. In the case of Na_2AuSb , there is a phonon gap throughout the Brillouin zone, except for an avoided crossing of bands around 5.4 THz along X direction. Nevertheless, the phonon bands are relatively flat which imply small phonon group velocities (v) and accordingly short phonon lifetime (τ). The low values of v and τ imply a low κ_L as they are related by the expression $\kappa_L = \frac{1}{3} C_v v^2 \tau$. The calculated phonon group velocity and lifetime as a function of frequency for both materials are shown in Fig. 5. As we observe from

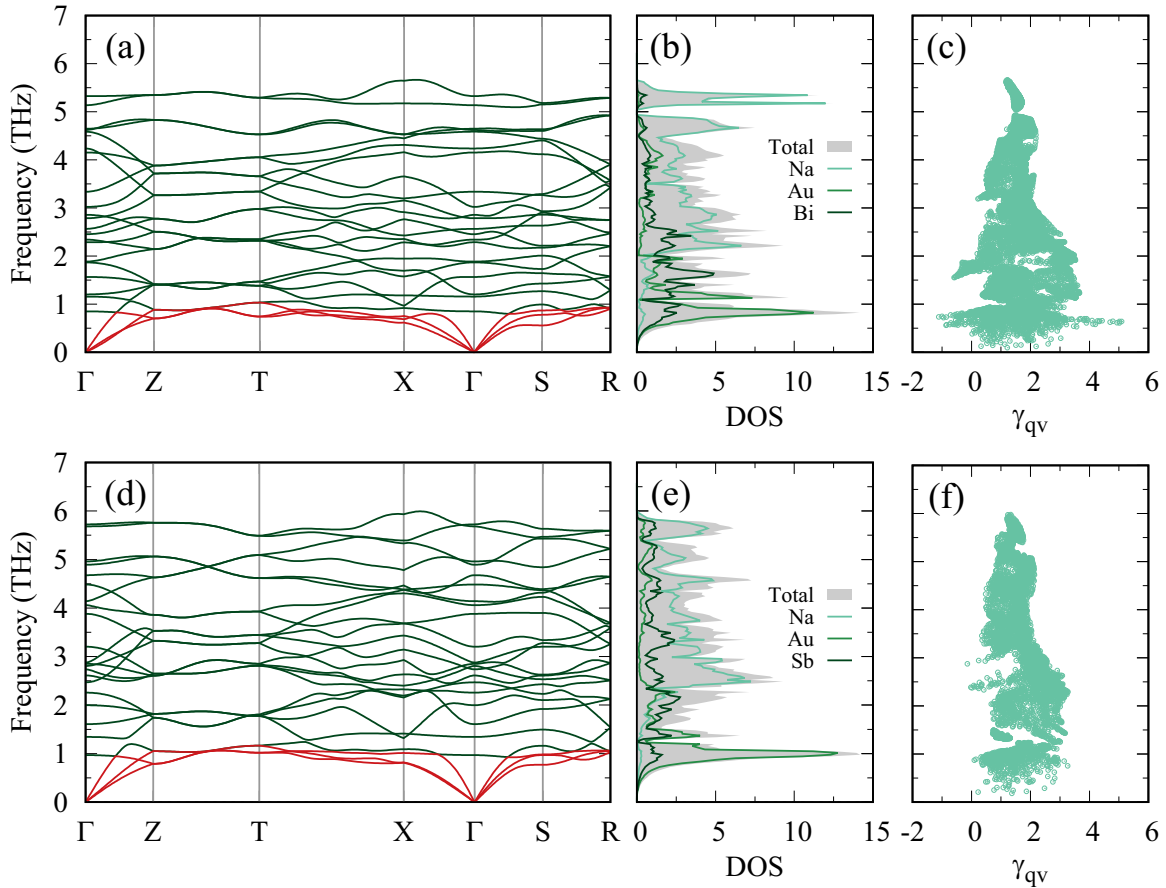


FIG. 4. Calculated [(a) and (d)] phonon dispersion curves, [(b) and (e)] partial phonon density of states, and [(c) and (f)] Grüneisen parameter of Na_2AuBi and Na_2AuSb , respectively, in $Cmcm$ symmetry.

the figure, the average group velocity in the acoustic region is $\sim 0.67 \text{ km s}^{-1}$ for Na_2AuBi and $\sim 0.69 \text{ km s}^{-1}$ for Na_2AuSb .

This implies that the heat carrying phonons are indeed slow. In fact, the v values are significantly lower than some low κ_L reported materials like SnSe (3.1 km s^{-1}) [41], Cu_3SbSe_4 [44] (2.2 km s^{-1}), and BiCuSeO (2.0 km s^{-1}) [45]. On the other hand, the low phonon lifetimes for both materials suggest frequent scattering of phonon modes. This further substantiates the low κ_L values. The room temperature lifetime of phonons ranges up to ~ 7 and 9 ps for Na_2AuBi and Na_2AuSb , respectively. Importantly, the lifetime of heat carrying phonons in the acoustic region is less than 5 ps for the majority of phonons.

To gain further insight into the κ_L , we calculated the mean square displacement (MSD) of atoms around their equilibrium position. In the literature, the larger value of room temperature atomic displacement parameter (ADP) is demonstrated to be associated with low κ_L [46]. The large ADP is a characteristic of host-guest type structures. However, the intrinsic large ADP and low κ_L is also observed in many compounds [17–19,21,22,47,48]. For instance, the room temperature low κ_L in TlInTe_2 is attributed to its large ADP (0.07 \AA^2) [22]. The calculated MSD for Na_2AuBi and Na_2AuSb from the present work is shown in Fig. 6. The large value for Na is expected on account of its lighter mass. However, the negligible contribution from Na to heat carrying phonons in the acoustic region makes it immaterial. Nevertheless, we obtained significant ADPs for Au in Na_2AuBi (0.03 \AA^2 at 300 K) and Na_2AuSb (0.02 \AA^2 at 300 K). Since the vibrations in the acoustic region are dominated by Au atoms,

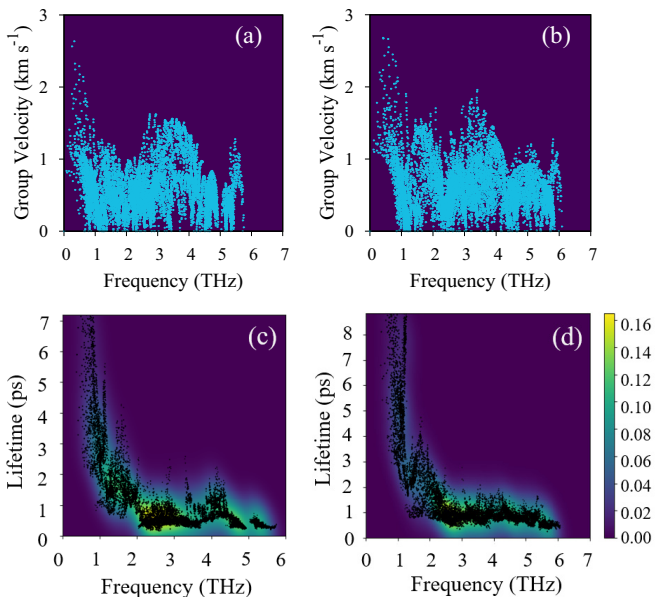


FIG. 5. Calculated [(a) and (b)] average group velocities and [(c) and (d)] phonon lifetime (at 300 K) of Na_2AuBi and Na_2AuSb , respectively. The color bar indicates the phonon density.

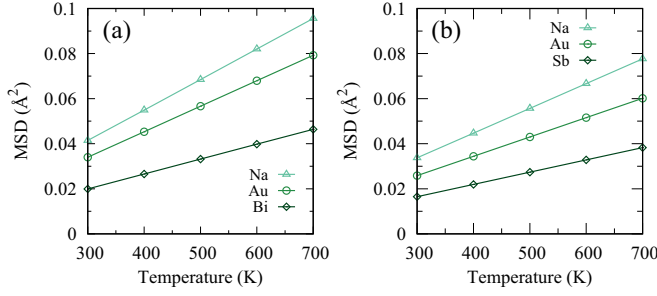


FIG. 6. Calculated average mean square displacements as a function of temperature of (a) Na_2AuBi and (b) Na_2AuSb .

it is customary to expect low κ_L in the proposed systems. The doping of K at the Na site seems reasonable. K is likely to have large ADP as it succeeds Na-atom, however, the effect may be less pronounced. Since K is heavier than Na, it may contribute to low-lying optical phonon modes, if not in the acoustic region. Thereby, suppressing the κ_L in both cases.

The low κ_L values also find their origin in anharmonicity. The quantitative estimation of anharmonicity in a crystal lattice is given by the Grüneisen parameter (γ), which represents the change in phonon frequencies with volume. Large γ values signify strong anharmonic lattice vibrations and low κ_L values. The Grüneisen parameter governed exceptionally low κ_L values are reported in SnSe ($\gamma \sim 7$) [40] and BaAgTe₃ ($\gamma \sim 7$) [17], to name a few. To obtain the γ , we calculated phonons at equilibrium, 2% larger, and 2% smaller volumes. The data from our calculations are shown in panels (c) and (f) of Fig. 4 for Na_2AuBi and Na_2AuSb , respectively. As we observe, the average value of the Grüneisen parameter in the acoustic region is $\gamma \sim 1.5$ and 1.7 for Na_2AuBi and Na_2AuSb , respectively. And, the maximum obtained values in the acoustic region are $\gamma \sim 5.0$ for Na_2AuBi and $\gamma \sim 3.1$ in the case of Na_2AuSb , illustrating some degree of anharmonicity.

Collectively, the features of Grüneisen parameter, atomic displacement parameters, phonon group velocities, lifetimes, and phonon dispersions demonstrate the low κ_L in Na_2AuBi and Na_2AuSb Zintl phases.

C. Electrical transport properties

Next, we examine the electrical transport parameters for Na_2AuBi and Na_2AuSb . It is to be however mentioned that the electrical transport properties are calculated using GGA-PBE due to the compute intensive nature of the mBJ calculations. The Seebeck coefficient, electrical conductivity, and electronic thermal conductivity are derived from the generalized transport coefficient as implemented in AMSET [34]. Mathematically, they are expressed as

$$S_{\alpha\beta} = \frac{1}{eT} \frac{\mathcal{L}_{\alpha\beta}^1}{\mathcal{L}_{\alpha\beta}^0}, \quad (3a)$$

$$\sigma_{\alpha\beta} = \mathcal{L}_{\alpha\beta}^0, \quad \text{and} \quad (3b)$$

$$\kappa_{\alpha\beta} = \left[\frac{1}{e^2 T} \frac{(\mathcal{L}_{\alpha\beta}^1)^2}{\mathcal{L}_{\alpha\beta}^0} - \mathcal{L}_{\alpha\beta}^2 \right], \quad (3c)$$

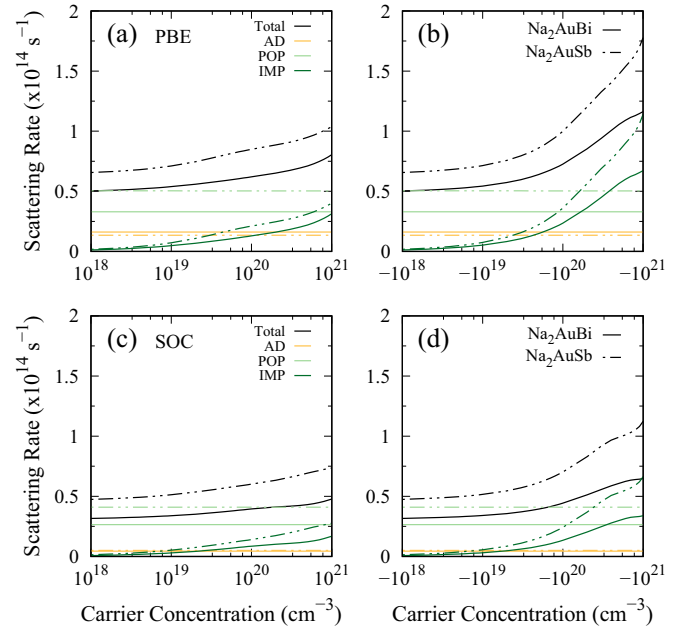


FIG. 7. Calculated scattering rates as a function of [(a) and (c)] p -type and [(b) and (d)] n -type carrier concentration for Na_2AuBi and Na_2AuSb using PBE and PBE-SOC.

respectively. Here, α and β represent the cartesian coordinates, e denotes the electronic charge, T is the temperature, and \mathcal{L} is the generalized transport coefficient, given as

$$\mathcal{L}_{\alpha\beta}^n = e^2 \int \sum_{\alpha\beta} (\varepsilon) (\varepsilon - \varepsilon_F)^n \left[-\frac{\partial f^0}{\partial \varepsilon} \right] d\varepsilon, \quad (4)$$

where ε_F is Fermi level at a particular doping, f^0 is the Fermi distribution function, and $\sum_{\alpha\beta} (\varepsilon)$ is the spectral conductivity, which relates to the scattering rate.

The scattering rate of charge carriers is a crucial parameter for governing the transport properties. It is derived from the data on the elastic constants, deformation potential, piezoelectric coefficient, polar optical phonon frequency, and static and high frequency dielectric constants. The contribution of the piezoelectric coefficient was negligible, hence, ignored for further calculations. In Fig. 7, we have shown the variation of different scattering rates with doping concentrations at room temperature. As discernible from the figure, the AD and POP scattering rates are almost constant throughout the selected doping range for both p - and n -type doping, with the contribution of POP is higher than AD. However, the IMP scattering rate increases steadily with the increasing carrier concentration. Though POP remains the dominant scattering mechanism for p -type doping, IMP dominates n -type doping at higher doping levels. Overall, the scattering rate expectedly increases with increasing carrier concentration. The total scattering rate ranges $0.3\text{--}1.75 \times 10^{14} \text{ s}^{-1}$.

As stated earlier, our interest lies in room temperature (300 K) thermoelectric applications, in Fig. 8, we have shown the electrical transport coefficients as a function of doping at 300 K for both materials. We would like to first discuss the results with PBE, followed by the effect of SOC on the properties. The Seebeck coefficient [panels (a) and (e)], in

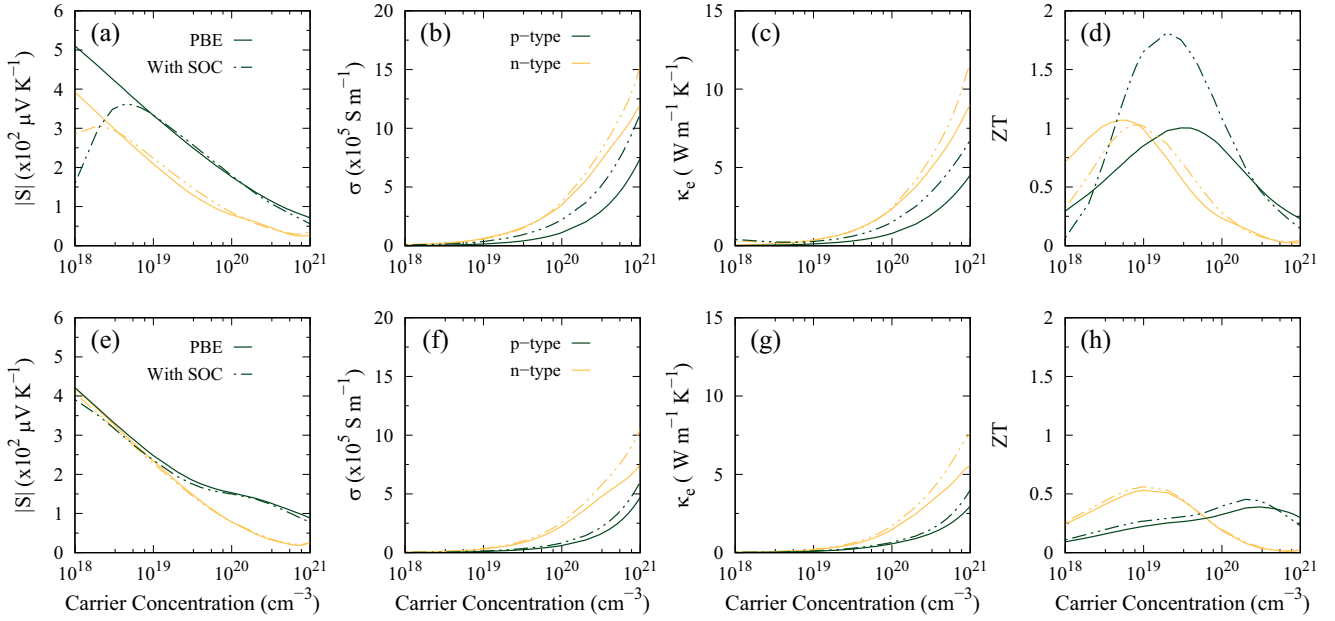


FIG. 8. Calculated [(a) and (e)] Seebeck coefficient, [(b) and (f)] electrical conductivity, [(c) and (g)] electronic thermal conductivity, [(d) and (h)] figure of merit as a function of carrier concentration at 300 K for Na_2AuBi and Na_2AuSb , respectively, using PBE and PBE-SOC.

accordance with the Mott equation [49,50], falls gradually at higher dopings, and the higher values of the Seebeck coefficient are obtained on p -type doping. On the other hand, the electrical conductivity increases with increasing carrier concentration on account of increased charge carriers [panels (b) and (f)]. The higher values of electrical conductivity are obtained on n -type doping. Importantly, the opposite trends of S and σ render the maximum power factor ($S^2\sigma$) near the band edge. We obtained the maximum power factor on p -type doping. Further, the electronic thermal conductivity follows a similar trend as that of σ [panels (c) and (g)]. Altogether, the conflicting electrical transport coefficients S , σ , and κ_e requires an optimal doping level to achieve the maximum efficiency. The directional dependent electrical transport properties are provided in Ref. [51].

To obtain the comprehensive thermoelectric figure of merit ZT , we used electrical transport coefficients (S , σ , and κ_e) at the proposed doping levels. As it is computationally expensive to compute κ_L for doped systems, we resort to the κ_L of the parent composition. Nevertheless, the thuswise obtained figure of merit for Na_2AuBi at 300 K is $ZT \sim 1.0$ for both p -type (3×10^{19} carriers cm^{-3}) and n -type (6×10^{18} carriers cm^{-3}) dopings. For Na_2AuSb , at 300 K, the $ZT \sim 0.38$ and 0.53 for p -type (3×10^{20} carriers cm^{-3}) and n -type (1×10^{19} carriers cm^{-3}) dopings, respectively. The predicted room temperature ZT values are certainly competitive with traditional thermoelectric materials such as Bi_2Te_3 ($ZT \sim 0.13$) [52] and PbTe ($ZT \sim 1$) [53].

Considering the impact of SOC on the electronic properties, next we examine its effect on the electrical transport properties. For Na_2AuSb , with the inclusion of SOC, we find negligible change in the Seebeck coefficient, whereas the electrical conductivity and electronic thermal conductivity gradually increase in the carrier concentration range 10^{20} to 10^{21} cm^{-3} . Overall, there is no significant change in the values of the figure of merit on either type of doping. In

case of Na_2AuBi , we obtain an initial increase in the Seebeck coefficient at low doping concentrations. Beyond that, the Seebeck coefficient falls gradually and matches well with the PBE results. The electrical conductivity and electronic thermal conductivity follow a similar trend as that of Na_2AuSb . However, it is important to note that the increase in electrical conductivity is more pronounced in the case of p -type Na_2AuBi which also reflects in its ZT value. While the ZT for n -type Na_2AuBi varies marginally with SOC, the ZT for p -type Na_2AuBi (2×10^{19} carriers cm^{-3}) has improved from 1 to 1.8. Further, the doping levels are quite pragmatic and can be achieved experimentally.

Moreover, it is important to note that the calculations are performed for the pristine system. The real material may have defects, grain boundaries, and other imperfections. This may result in even lower thermal conductivity, and hence higher ZT values. Altogether, we have shown the importance of Na_2AuBi and Na_2AuSb as promising thermoelectric candidates. We are hopeful that our predictions would encourage experimentalists to explore the thermoelectric properties in the proposed systems.

IV. CONCLUSION

With the help of first-principles calculations, we have demonstrated the thermoelectric potential of Zintl phases Na_2AuBi and Na_2AuSb . Both systems crystallize in orthorhombic $Cmcm$ symmetry and are semiconducting with indirect and direct band gaps of 0.30 and 0.33 eV, respectively. The values are reduced to 0.14 and 0.23 eV, respectively, with the inclusion of the spin-orbit coupling. The corrected band gaps using mBJ potential are 0.89 and 0.97 eV, respectively. The electronic features suggest promising electrical transport properties on account of degenerate bands near the Fermi level. The key finding for both materials is low lattice thermal

conductivity like other Zintl phases. We attribute such low κ_L values to low phonon group velocities in the acoustic region, significant atomic displacement parameter, and lattice anharmonicity. Based on such low thermal conductivity values, we find high room-temperature figure of merit, i.e., $ZT \sim 1$ for Na_2AuBi and 0.53 for Na_2AuSb at 300 K. The value is significantly improved for Na_2AuBi with spin-orbit coupling, i.e., $ZT \sim 1.8$. We are optimistic that our findings would motivate experimentalists to explore the thermoelectric properties of the hitherto unexplored Na_2AuBi and Na_2AuSb .

ACKNOWLEDGMENTS

M.Z. and C.K.V. are thankful to MHRD and CSIR, respectively, for their financial assistance. M.Z. gratefully acknowledges Prof. Hem C. Kandpal, IIT Roorkee, for useful discussion. B.K.M. acknowledges the funding support from the SERB, DST (ECR/2016/001454). The results presented in the paper are based on the computations using the High Performance Computing cluster, Padum, at the Indian Institute of Technology Delhi.

-
- [1] P. Gorai, A. Ganose, A. Faghaninia, A. Jain, and V. Stevanović, Computational discovery of promising new n-type dopable ABX Zintl thermoelectric materials, *Mater. Horiz.* **7**, 1809 (2020).
- [2] J. W. Bennett, K. F. Garrity, K. M. Rabe, and D. Vanderbilt, Orthorhombic ABC Semiconductors as Antiferroelectrics, *Phys. Rev. Lett.* **110**, 017603 (2013).
- [3] A. Roy, J. W. Bennett, K. M. Rabe, and D. Vanderbilt, Half-Heusler Semiconductors as Piezoelectrics, *Phys. Rev. Lett.* **109**, 037602 (2012).
- [4] B. B. Iversen, Breaking thermoelectric performance limits, *Nat. Mater.* **20**, 1309 (2021).
- [5] B. Jiang, Y. Yu, H. Chen, J. Cui, X. Liu, L. Xie, and J. He, Entropy engineering promotes thermoelectric performance in p-type chalcogenides, *Nat. Commun.* **12**, 3234 (2021).
- [6] P. Acharyya, S. Roychowdhury, M. Samanta, and K. Biswas, Ultralow thermal conductivity, enhanced mechanical stability, and high thermoelectric performance in $(\text{GeTe})_{1-2x}(\text{SnSe})_x(\text{SnS})_x$, *J. Am. Chem. Soc.* **142**, 20502 (2020).
- [7] F. Garmroudi, A. Riss, M. Parzer, N. Reumann, H. Müller, E. Bauer, S. Khmelevskiy, R. Podloucky, T. Mori, K. Tobita, Y. Katsura, and K. Kimura, Boosting the thermoelectric performance of Fe_2VAI -type Heusler compounds by band engineering, *Phys. Rev. B* **103**, 085202 (2021).
- [8] S. Karmakar and T. Saha-Dasgupta, First-principles prediction of enhanced thermoelectric properties of double transition metal MXenes: $\text{Ti}_{3-x}\text{Mo}_x\text{C}_2\text{T}_2$; ($x = 0.5, 1, 1.5, 2, 2.5$, $T = -\text{OH}/-\text{O}/-\text{F}$), *Phys. Rev. Materials* **4**, 124007 (2020).
- [9] J. Maassen, Limits of thermoelectric performance with a bounded transport distribution, *Phys. Rev. B* **104**, 184301 (2021).
- [10] M. Zeeshan, T. Nautiyal, J. van den Brink, and H. C. Kandpal, FeTaSb and FeMnTiSb as promising thermoelectric materials: An *ab initio* approach, *Phys. Rev. Materials* **2**, 065407 (2018).
- [11] T. Berry, C. Fu, G. Auffermann, G. H. Fecher, W. Schnelle, F. Serrano-Sanchez, Y. Yue, H. Liang, and C. Felser, Enhancing thermoelectric performance of TiNiSn half-Heusler compounds via modulation doping, *Chem. Mater.* **29**, 7042 (2017).
- [12] S. R. Boona, Nanomagnets boost thermoelectric output, *Nature (London)* **549**, 169 (2017).
- [13] Y. K. Lee, K. Ahn, J. Cha, C. Zhou, H. S. Kim, G. Choi, S. I. Chae, J.-H. Park, S.-P. Cho, S. H. Park, Y.-E. Sung, W. B. Lee, T. Hyeon, and I. Chung, Enhancing p-type thermoelectric performances of polycrystalline SnSe via tuning phase transition temperature, *J. Am. Chem. Soc.* **139**, 10887 (2017).
- [14] G. Tan, S. Hao, J. Zhao, C. Wolverton, and M. G. Kanatzidis, High thermoelectric performance in electron-doped AgBi_3S_5 with ultralow thermal conductivity, *J. Am. Chem. Soc.* **139**, 6467 (2017).
- [15] L. E. Bell, Cooling, heating, generating power, and recovering waste heat with thermoelectric systems, *Science* **321**, 1457 (2008).
- [16] J. Yu, C. Fu, Y. Liu, K. Xia, U. Aydemir, T. C. Chasapis, G. J. Snyder, X. Zhao, and T. Zhu, Unique role of refractory Ta alloying in enhancing the figure of merit of NbFeSb thermoelectric materials, *Adv. Energy Mater.* **8**, 1701313 (2018).
- [17] K. Pal, Y. Xia, J. He, and C. Wolverton, High thermoelectric performance in BaAgYTe_3 via low lattice thermal conductivity induced by bonding heterogeneity, *Phys. Rev. Materials* **3**, 085402 (2019).
- [18] M. K. Jana, K. Pal, U. V. Waghmare, and K. Biswas, The origin of ultralow thermal conductivity in InTe : Lone-pair-induced anharmonic rattling, *Angew. Chem. Int. Ed.* **55**, 7792 (2016).
- [19] M. Dutta, S. Matteppanavar, M. V. D. Prasad, J. Pandey, A. Warankar, P. Mandal, A. Soni, U. V. Waghmare, and K. Biswas, Ultralow thermal conductivity in chain-like TlSe due to inherent TI^+ rattling, *J. Am. Chem. Soc.* **141**, 20293 (2019).
- [20] E. S. Toberer, A. Zevkink, N. Crisosto, and G. J. Snyder, The Zintl compound $\text{Ca}_5\text{Al}_2\text{Sb}_6$ for low-cost thermoelectric power generation, *Adv. Funct. Mater.* **20**, 4375 (2010).
- [21] D. J. Voneshen, K. Refson, E. Borissenko, M. Krisch, A. Bosak, A. Piovano, E. Cemal, M. Enderle, M. J. Gutmann, M. Hoesch, M. Roger, L. Gannon, A. T. Boothroyd, S. Uthayakumar, D. G. Porter, and J. P. Goff, Suppression of thermal conductivity by rattling modes in thermoelectric sodium cobaltate, *Nat. Mater.* **12**, 1028 (2013).
- [22] M. K. Jana, K. Pal, A. Warankar, P. Mandal, U. V. Waghmare, and K. Biswas, Intrinsic rattler-induced low thermal conductivity in Zintl type TlInTe_2 , *J. Am. Chem. Soc.* **139**, 4350 (2017).
- [23] S. M. Kauzlarich, S. R. Brown, and G. Jeffrey Snyder, Zintl phases for thermoelectric devices, *Dalton Trans.* **21**, 2099 (2007).
- [24] S.-J. Kim, J. R. Ireland, C. R. Kannewurf, and M. G. Kanatzidis, $\text{Yb}_5\text{In}_2\text{Sb}_6$: A new rare earth Zintl phase with a narrow band gap, *J. Solid State Chem.* **155**, 55 (2000).
- [25] S. Huang, H. J. Liu, D. D. Fan, P. H. Jiang, J. H. Liang, G. H. Cao, R. Z. Liang, and J. Shi, First-principles study of the thermoelectric properties of the Zintl compound KSnSb , *J. Phys. Chem. C* **122**, 4217 (2018).
- [26] S.-J. Kim, G. J. Miller, and J. D. Corbett, Zigzag chains of alternating atoms in A_2AuBi ($\text{A} = \text{Na}, \text{K}$) and K_2AuSb . Synthesis, structure, and bonding, *Z. anorg. allg. Chem.* **636**, 67 (2010).

- [27] C. Mues and H.-U. Schuster, Na_2AuAs , Na_2AuSb , K_2AuSb - drei neue A_2BX -Verbindungen mit B-X-Kettenstruktur / Na_2AuAs , Na_2AuSb , K_2AuSb - Three new A_2BX compounds with a B-X chain structure, *Zeitschrift für Naturforschung B* **35**, 1055 (1980).
- [28] G. Xing, J. Sun, Y. Li, X. Fan, W. Zheng, and D. J. Singh, Electronic fitness function for screening semiconductors as thermoelectric materials, *Phys. Rev. Materials* **1**, 065405 (2017).
- [29] G. Kresse and J. Furthmüller, Efficiency of *ab-initio* total energy calculations for metals and semiconductors using a plane-wave basis set, *Comput. Mater. Sci.* **6**, 15 (1996).
- [30] G. Kresse and J. Furthmüller, Efficient iterative schemes for *ab initio* total-energy calculations using a plane-wave basis set, *Phys. Rev. B* **54**, 11169 (1996).
- [31] J. P. Perdew, K. Burke, and M. Ernzerhof, Generalized Gradient Approximation Made Simple, *Phys. Rev. Lett.* **77**, 3865 (1996).
- [32] A. Togo and I. Tanaka, First principles phonon calculations in materials science, *Scr. Mater.* **108**, 1 (2015).
- [33] A. Togo, L. Chaput, and I. Tanaka, Distributions of phonon lifetimes in Brillouin zones, *Phys. Rev. B* **91**, 094306 (2015).
- [34] A. M. Ganose, J. Park, A. Faghaninia, R. Woods-Robinson, K. A. Persson, and A. Jain, Efficient calculation of carrier scattering rates from first principles, *Nat. Commun.* **12**, 2222 (2021).
- [35] C. Stampfl and C. G. Van de Walle, Density-functional calculations for III-V nitrides using the local-density approximation and the generalized gradient approximation, *Phys. Rev. B* **59**, 5521 (1999).
- [36] F. Tran and P. Blaha, Accurate Band Gaps of Semiconductors and Insulators with a Semilocal Exchange-Correlation Potential, *Phys. Rev. Lett.* **102**, 226401 (2009).
- [37] Y. Tang, Z. M. Gibbs, L. A. Agapito, G. Li, H.-S. Kim, M. B. Nardelli, S. Curtarolo, and G. J. Snyder, Convergence of multi-valley bands as the electronic origin of high thermoelectric performance in CoSb_3 skutterudites, *Nat. Mater.* **14**, 1223 (2015).
- [38] L. Zhang, M.-H. Du, and D. J. Singh, Zintl-phase compounds with SnSb_4 tetrahedral anions: Electronic structure and thermoelectric properties, *Phys. Rev. B* **81**, 075117 (2010).
- [39] W. Li, G. Yang, and J. Zhang, Optimization of the thermoelectric properties of FeNbSb-based half-Heusler materials, *J. Phys. D: Appl. Phys.* **49**, 195601 (2016).
- [40] L.-D. Zhao, S.-H. Lo, Y. Zhang, H. Sun, G. Tan, C. Uher, C. Wolverton, V. P. Dravid, and M. G. Kanatzidis, Ultralow thermal conductivity and high thermoelectric figure of merit in SnSe crystals, *Nature (London)* **508**, 373 (2014).
- [41] R. Guo, X. Wang, Y. Kuang, and B. Huang, First-principles study of anisotropic thermoelectric transport properties of IV-VI semiconductor compounds SnSe and SnS , *Phys. Rev. B* **92**, 115202 (2015).
- [42] B.-L. Huang and M. Kaviani, *Ab initio* and molecular dynamics predictions for electron and phonon transport in bismuth telluride, *Phys. Rev. B* **77**, 125209 (2008).
- [43] B. Peng, H. Zhang, H. Shao, Y. Xu, G. Ni, R. Zhang, and H. Zhu, Phonon transport properties of two-dimensional group-IV materials from *ab initio* calculations, *Phys. Rev. B* **94**, 245420 (2016).
- [44] Y. Zhang, E. Skoug, J. Cain, V. Ozoliņš, D. Morelli, and C. Wolverton, First-principles description of anomalously low lattice thermal conductivity in thermoelectric Cu-Sb-Se ternary semiconductors, *Phys. Rev. B* **85**, 054306 (2012).
- [45] L.-D. Zhao, J. He, D. Berardan, Y. Lin, J.-F. Li, C.-W. Nan, and N. Dragoë, BiCuSeO oxyselenides: New promising thermoelectric materials, *Energy Environ. Sci.* **7**, 2900 (2014).
- [46] B.C. Sales, B.C. Chakoumakos, D. Mandrus, and J.W. Sharp, Atomic displacement parameters and the lattice thermal conductivity of clathrate-like thermoelectric compounds, *J. Solid State Chem.* **146**, 528 (1999).
- [47] S. Mukhopadhyay, D. S. Parker, B. C. Sales, A. A. Puretzky, M. A. McGuire, and L. Lindsay, Two-channel model for ultralow thermal conductivity of crystalline Ti_3VSe_4 , *Science* **360**, 1455 (2018).
- [48] C. Chen, Z. Feng, H. Yao, F. Cao, B.-H. Lei, Y. Wang, Y. Chen, D. J. Singh, and Q. Zhang, Intrinsic nanostructure induced ultralow thermal conductivity yields enhanced thermoelectric performance in Zintl phase Eu_2ZnSb_2 , *Nat. Commun.* **12**, 5718 (2021).
- [49] J. P. Heremans, V. Jovovic, E. S. Toberer, A. Saramat, K. Kurosaki, A. Charoenphakdee, S. Yamanaka, and G. J. Snyder, Enhancement of thermoelectric efficiency in PbTe by distortion of the electronic density of states, *Science* **321**, 554 (2008).
- [50] M. Cutler and N. F. Mott, Observation of Anderson localization in an electron gas, *Phys. Rev.* **181**, 1336 (1969).
- [51] See Supplemental Material at <http://link.aps.org/supplemental/10.1103/PhysRevMaterials.6.085404> for directional dependent electrical transport properties of Na_2AuBi and Na_2AuSb with PBE and PBE-SOC.
- [52] N. Gothard, X. Ji, J. He, and T. M. Tritt, Thermoelectric and transport properties of n-type Bi_2Te_3 nanocomposites, *J. Appl. Phys.* **103**, 054314 (2008).
- [53] Y.-L. Pei and Y. Liu, Electrical and thermal transport properties of Pb-based chalcogenides: PbTe , PbSe , and PbS , *J. Alloys Compd.* **514**, 40 (2012).